Research Square

Preprints are preliminary reports that have not undergone peer review.
They should not be considered conclusive, used to inform clinical practice,
or referenced by the media as validated information.

Self-Sensing Piezoelectric Microcantilever Mass Sensor Based on Graphene Platelet- Reinforced Composite: Performance in Air and Liquid

Reza Ghaderi

Reza.ghaderi@iau.ac.ir

Islamic Azad University

Research Article

Keywords: Microcantilever, Mass sensor, Graphene platelet-reinforced composite, Piezoelectric self-sensing, Output current, Sobol sensitivity analysis, Liquid environment

Posted Date: November 12th, 2026

DOI: https://doi.org/10.21203/rs.3.rs-11502571/v1

License: This work is licensed under a Creative Commons Attribution 4.0 International License.
Read Full License

Additional Declarations: No competing interests reported.

Self-Sensing Piezoelectric Microcantilever Mass Sensor Based on Graphene Platelet-Reinforced Composite: Performance in Air and Liquid

Reza Ghaderi
Department of Mechanical Engineering, Shk.C, Islamic Azad University, Shahrekord, Iran
Reza.ghaderi@iau.ac.ir

Abstract

Resonant microcantilevers (MCs) are used for mass sensing, but their performance depends on the beam material and the surrounding medium. This paper presents a study of a self-actuating, self-sensing piezoelectric MC with a non-uniform geometry and a multilayer graphene platelet-reinforced composite (GPLRC) host structure. The model, based on Euler–Bernoulli beam theory and Hamilton's principle, includes the hydrodynamic loading of the liquid and uses the output current of the piezoelectric layer as the sensing signal. It was validated against experimental data in air and in water–glycerol mixtures, with deviations of about 2% in frequency in air and below 5.1% in liquids. The relative current change ΔI/I caused by a 20 ng nanoparticle was evaluated for four GPL distribution patterns, three polymer matrices (epoxy, polyamide 6, and polypropylene), and different GPL contents and liquids. In air, ΔI/I reaches about 22% under the baseline conditions, whereas in water it is about one order of magnitude smaller (1.1–2.4%). The O-GPLRC pattern gave the highest sensitivity in both media, while the matrix had only a small effect. A Sobol sensitivity analysis showed that the GPL width and thickness dominate the variance of ΔI/I, whereas the GPL length contributes only 2–5%.

Keywords: Microcantilever; Mass sensor; Graphene platelet-reinforced composite; Piezoelectric self-sensing; Output current; Sobol sensitivity analysis; Liquid environment

1. Introduction

Resonant microcantilevers (MCs) are among the most widely used transducers for detecting minute masses, because the adsorption of an analyte changes the effective mass of the beam and shifts its resonance characteristics [1-3]. Since the response of an MC is governed by its stiffness and mass distribution, the choice of beam material is a central design issue, and functionally graded and nanocomposite beams have been proposed to tune it [4]. For example, Formica et al. [5] proposed an array of carbon-nanotube nanocomposite microcantilevers for multi-mass sensing. They tuned the frequencies through the CNT volume fraction and showed that nonlinear frequency shifts improve the detectability of the added mass.

The readout method also matters. A piezoelectric layer can excite the MC and convert its vibration into an electrical signal, so that the device is self-actuating and self-sensing. In this configuration the output current of the piezoelectric layer serves as the sensing parameter, and it depends on the beam geometry and on the vibration mode [6, 7]. Shahraki and Ghaderi [6] modeled the output current of a self-sensing piezoelectric MC in air and in liquid, using the string-of-spheres model for the hydrodynamic force. They applied the Sobol method to the geometric parameters and found that the output drops in liquid and that denser liquids make the drop stronger. Because biosensing requires operation in liquid, where the fluid adds mass and viscous damping [8], a sensor should be evaluated in both air and liquid.

The MC material is another effective design variable. Graphene platelets (GPLs) are attractive nanofillers because of their very high stiffness [9] and their strong reinforcing effect at low content [10]. The properties of graphene-based composites depend on the filler content, dispersion, and matrix [11-13], and epoxy and polyamide are the most commonly studied matrices [14-16]. Polypropylene is a softer and lighter alternative, but its use as a GPL matrix in resonant sensors is less explored.

A further step is to grade the GPL content through the thickness, which gives functionally graded GPL-reinforced composites (FG-GPLRCs) [17, 18]. Feng et al. [19] studied the nonlinear free vibration of FG GPL-reinforced beams, and Song et al. [20] analyzed the free and forced vibration of FG GPL-reinforced plates. Both works showed that the GPL distribution pattern strongly affects the dynamic behavior. These findings were later extended to beams with dielectric properties, to size-dependent and axially graded microbeams, and to experimental modal testing [21-24].

GPLRCs have also been combined with piezoelectric layers to build smart structures. Mao et al. [25] studied the vibration of a GPL-reinforced functionally gradient piezoelectric microplate with nonlocal theory, and further works treated laminated microplates under thermoelectrical loads [26], active vibration control [27], electro-thermal vibration [28], and data-driven prediction [29]. Chen et al. [27], for example, investigated GPL-reinforced metal foam piezoelectric beams with velocity feedback control. These studies deal mainly with free vibration, buckling, or active control. The mass-sensing performance of a piezoelectric GPLRC microcantilever, in particular the output-current change caused by an adsorbed nanoparticle in air and in liquid, has received little attention.

To identify the parameters that control the response, global sensitivity analysis based on the Sobol method is well suited, since it quantifies the contribution of each input to the output variance, including interaction effects. The total-order indices can be estimated efficiently with the Saltelli scheme [30]. The method has been applied to the geometry of piezoelectric microcantilevers and to their vibration in liquid [6–8], but, to the authors' knowledge, not to the GPL geometric parameters of a GPLRC mass microsensor.

In this study, a self-sensing, self-actuating piezoelectric MC with a multilayer GPLRC host structure and a non-uniform geometry is modeled for mass sensing in air and liquid. The model, based on Euler–Bernoulli beam theory and Hamilton's principle, includes the hydrodynamic loading of the liquid and is validated against experimental data. The output current of the piezoelectric layer is the sensing signal, and the relative current change $\Delta I/I$ after the adsorption of a nanoparticle is the performance indicator. The effects of four GPL distribution patterns (U-, X-, O-, and A-GPLRC), three polymer matrices (epoxy, PA6, and PP), the GPL weight fraction, and the liquid properties on $\Delta I/I$ are examined. Finally, a Sobol-based global sensitivity analysis of the GPL length, width, and thickness identifies the dominant design parameters.

2. Constitutive Modeling of Multilayer GPLRC Microcantilevers

This work examines the free-vibration behavior of a multilayer graphene platelet-reinforced composite (GPLRC) microcantilever (MC) that incorporates an active piezoelectric actuation layer. The host structure of the MC is built from several GPLRC laminae of equal thickness, which are assumed to be perfectly bonded so that strain continuity is maintained across all interfaces. Every lamina consists of an isotropic polymer matrix filled with graphene platelets (GPLs); the platelets are taken to be randomly oriented and homogeneously dispersed within the plane of the matrix.

In order to tune the mechanical response of the MC, four GPL distribution schemes are adopted: a uniform pattern (U-GPLRC) and three functionally graded patterns, denoted A-GPLRC, X-GPLRC, and O-GPLRC (see Figure 1). In the figure, the shaded layers indicate those with a higher GPL content. Because the effective properties of the composite depend strongly on how the nanofillers are spatially arranged, such grading schemes offer an efficient way to control the through-thickness stiffness profile of the laminate and thereby to alter the dynamic behavior of the MC.



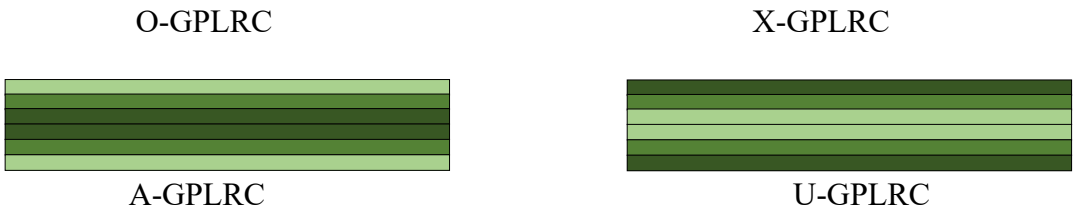


Figure 1. Schematic of the GPL distribution schemes considered for the multilayer GPLRC MC.

For the multilayer formulation, the GPLRC laminate is assumed to be made up of an even number of layers. The GPL volume fraction of the *n*th layer depends on the adopted distribution scheme in Figure 1 and is given by [19, 20]:

A-GPLRC: $$V_{GPL}^{i} = V_{GPL}^{T}|2i-1|/n \tag{1}$$

O-GPLRC: $$V_{GPL}^{i} = 2V_{GPL}^{T}(1-|2i-n_T-1|/n) \tag{2}$$

X-GPLRC: $$V_{GPL}^{i} = 2V_{GPL}^{T}|2i-n_T-1|/n \tag{3}$$

U-GPLRC: $$V_{GPL}^{i} = V_{GPL}^{T} \tag{4}$$

where V_{GPL}^{i} is the GPL volume fraction in the *i*th layer and *n* is the total number of layers in the laminate. The overall GPL volume fraction of the laminate is obtained from

$$V_{GPL}^{T} = \frac{W_{GPL}}{W_{GPL} + (\rho_{GPL}/\rho_m)(1-W_{GPL})} \tag{5}$$

where ρ_{GPL} and ρ_m are the densities of the graphene platelets and the polymer matrix, respectively, and W_{GPL} is the total GPL weight fraction of the composite. Although the overall GPL content is kept fixed, its distribution through the laminate thickness differs from one grading pattern to another.

The effective Young's modulus of each GPLRC layer is calculated with the modified Halpin–Tsai micromechanical model, which incorporates the geometric features and size effects of the graphene nanoplatelets [19, 20]. On this basis, the equivalent Young's modulus of the *i*th layer is given by:

$$E_i = \frac{E_m}{8}\left(3\frac{1+\alpha_1\lambda_1 V_{GPL}^{i}}{1-\lambda_1 V_{GPL}^{i}} + 5\frac{1+\alpha_2\lambda_2 V_{GPL}^{i}}{1-\lambda_2 V_{GPL}^{i}}\right) \tag{6}$$

where the parameters ζ_1 and ζ_2 are given by

$$\lambda_1 = \frac{E_{GPL}/E_m - 1}{E_{GPL}/E_m + \xi_1};\ \lambda_2 = \frac{E_{GPL}/E_m - 1}{E_{GPL}/E_m + \xi_2} \tag{7}$$

In these equations, E_{GPL} and E_m are the Young's moduli of the graphene platelets and the polymer matrix, respectively. The geometric parameters of the GPLs are given by

$$\xi_1 = \frac{2L_{GPL}}{h_{GPL}};\ \xi_2 = \frac{2b_{GPL}}{h_{GPL}} \tag{8}$$

where L_{GPL}, b_{GPL}, and h_{GPL} denote the length, width, and thickness of the graphene platelets, respectively. The effective Poisson's ratio of each GPLRC layer is determined using the classical rule of mixtures as

$$\upsilon = \upsilon_m V_m + \upsilon_{GPL} V_{GPL} \tag{9}$$

where ν_{GPL} and ν_m denote the Poisson's ratios of the graphene platelets and matrix, respectively. Thus, the mechanical properties of each GPLRC layer are determined according to its local GPL content, while the overall GPL content of the laminate remains constant for all considered distribution patterns. This formulation

enables the effects of different through-thickness GPL distributions on the dynamic response of the piezoelectric MC to be investigated within a unified multilayer framework.

3. Electromechanical Modeling of the Piezoelectric GPLRC MC for Mass Sensing

The MC under study has a non-uniform geometry and contains an active piezoelectric layer that provides the electromechanical excitation. Its structural part is a multilayer GPLRC laminate, whereas the piezoelectric layer is sandwiched between the top and bottom electrodes. When an alternating voltage is applied across the electrodes, the piezoelectric layer drives transverse vibration of the MC through electromechanical coupling. The MC is fixed at one end, and its geometry tapers into a sharp, narrowed region close to the free end, a configuration well suited to mass sensing.

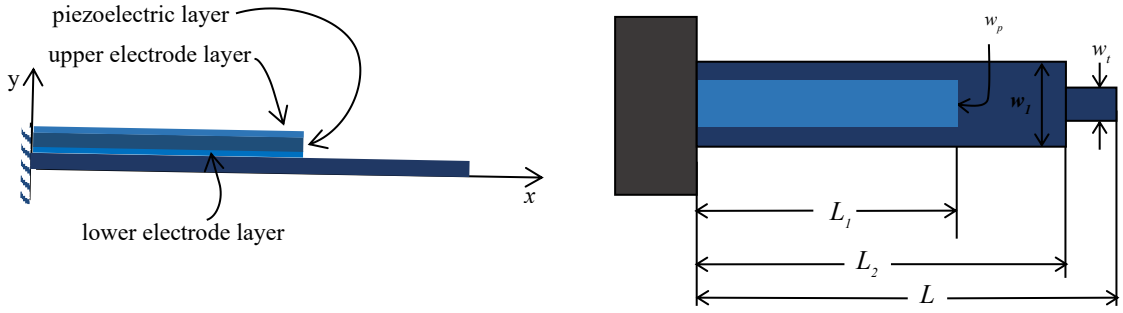


Figure 2. Schematic configuration of the piezoelectric GPLRC MC

Based on the Euler–Bernoulli beam theory, the equation of motion of the MC with geometric discontinuities is derived using an energy approach. The kinetic and potential energies of the structure, including the contributions of the multilayer GPLRC laminate, the piezoelectric layer, and the attached mass, are expressed in terms of the transverse deflection *w(x,t)*. Applying Hamilton's principle and the Lagrange method, and accounting for the abrupt variations in the cross-sectional properties along the length through step functions, the governing partial differential equation of the transverse vibration is obtained as:

$$m_0(x)\frac{\partial^2 v(x,t)}{\partial x^2}+\frac{\partial^2}{\partial x^2}\left[K(x)\frac{\partial^2 v(x,t)}{\partial x^2}\right]+C\frac{\partial v(t)}{\partial t}+\frac{\partial^2 C_P(x)}{\partial x^2}P(t)=0 \tag{10}$$

where P(t) is the alternating input voltage applied across the electrodes of the piezoelectric layer, which drives the transverse vibration of the MC through the electromechanical coupling.

The equivalent mass per unit length, $m_0(x)$ is

$$m_0(x)=\sum_{j=1}^{n+3}\rho_j w_j h_j\left(H_0-H_{L_1}\right)+\sum_{j=1}^{n}\rho_j w_j h_j\left(H_{L_1}-H_{L_2}\right)+\rho_1 w_t h_1\left(H_{L_2}-H_L\right) \tag{11}$$

Here ρ, w, and h are the density, width, and thickness of each layer, respectively, w_t is the tip width of the MC, and $H(x)$ is the Heaviside step function, with $H_L = H(x\text{-}L)$.

The MC has three regions: the multilayer GPLRC-piezoelectric region, the GPLRC-only region, and the narrowed tip region. Its bending stiffness over these regions is

$$K(x)=K_1(H_0-H_{L_1})+K_2(H_{L_1}-H_{L_2})+K_3(H_{L_2}-H_L) \tag{12}$$

where

$$K_1 = \sum_{k=1}^{n+3} E_k w_k h_k \left\{ \frac{w_k^2}{12} + \left[y_n - \left(\sum_{j=1}^{n+3} w_j - \frac{w_k}{2} \right) \right]^2 \right\} \tag{13}$$

$$K_2 = \sum_{k=1}^{n} E_k w_k h_k \left\{ \frac{w_k^2}{12} + \left[y_{GPL} - \left(\sum_{j=1}^{n} w_j - \frac{w_k}{2} \right) \right]^2 \right\} \tag{14}$$

$$K_3 = w_t \sum_{k=1}^{n_L} E_k h_k \left\{ \frac{w_k^2}{12} + \left[y_{GPL} - \left(\sum_{j=1}^{n} w_j - \frac{w_k}{2} \right) \right]^2 \right\} \tag{15}$$

The neutral-axis position of the multilayer cross-section (y_n) and that of the GPLRC layers (y_{GPL}) are given by

$$y_n = \sum_{k=1}^{n+3} E_k w_k h_k \left(\sum_{j=1}^{k} h_j - \frac{h_k}{2} \right) / \sum_{k=1}^{n+3} E_k w_k h_k \tag{16}$$

$$y_{GPL} = \sum_{k=1}^{n} E_i w_i h_i \left(\sum_{j=1}^{k} h_j - \frac{h_k}{2} \right) / \sum_{k=1}^{n} E_k w_k h_k \tag{17}$$

The electromechanical coupling coefficient of the piezoelectric layer is

$$C_P = \frac{1}{2} E_P d_{31} w_P \left(\sum_{k=1}^{n+3} h_k - \frac{h_p}{2} - y_n \right) \left(H_0 - H_{L_1} \right) \tag{18}$$

where w_P and h_P are the width and thickness of the piezoelectric layer, respectively, and E_p is the Young's modulus of the piezoelectric layer.

The MC is clamped at $x = 0$ and free at $x = L$, and the attached nanoparticle with mass, m_p, is assumed to be concentrated at the free end. The boundary conditions are therefore

$$\begin{aligned} &v(0,t) = 0 \\ &v'(0,t) = 0 \\ &v''(L,t) = 0 \end{aligned} \tag{19}$$

$$K(L) \frac{\partial^3 v(x,L)}{\partial x^3} = m_p \frac{\partial^2 v(x,t)}{\partial x^2} \tag{20}$$

Together with the piecewise bending stiffness and mass distributions, these boundary conditions complete the dynamic model of the piezoelectric GPLRC MC. This model is the basis for the subsequent modal analysis and the evaluation of its mass-sensing characteristics.

In an air environment, the damping coefficient C of the MC mainly arises from its interaction with the surrounding air and can be estimated through modal analysis using the experimentally measured quality factor. In a liquid environment, the dynamic response is more complicated, because the surrounding fluid adds hydrodynamic loading. In particular, the fluid force produced by the compression and displacement of the liquid near the MC surface affects both the effective inertia and the damping of the structure. These effects

matter most in biosensing applications, where the MC operates while immersed in liquid and may vibrate close to the container bottom. In that case, confined-fluid effects can further resist the motion of the cantilever.

Two general approaches have been used to model the vibration of an MC in liquid. The first is the inviscid-fluid formulation, which neglects the viscosity of the liquid and is generally adequate when viscous effects are sufficiently weak. The second approach includes the fluid viscosity explicitly in the vibration model. Among the available viscous formulations, the string-of-spheres model offers a convenient description of fluid-structure interaction, since it accounts for both viscous and hydrodynamic effects [31]. In this model, the MC is represented as a string of interconnected spheres, and the fluid forces acting on the spheres are transmitted to the cantilever. The hydrodynamic force on the MC is then given by:

$$F_h(x,t) = -\left(0.6\rho_{liq}L_i^{0.5}w^{1.5}\right)\ddot{v} - \left(3\pi\eta + \frac{3}{4}\pi w^2\sqrt{2\eta\rho_{liq}\Omega}\right)\dot{v} \tag{21}$$

where ρ_{liq} and η are the density and dynamic viscosity of the surrounding liquid, respectively. In this study, Ω is taken as the resonance frequency of the MC, which is consistent with biosensor operation under resonant excitation.

As Eq. (21) shows, the fluid-induced damping and compression forces depend on the local velocity and acceleration of the MC, respectively. Their effects can therefore be included in the governing differential equation, Eq. (10), by modifying the damping and inertia terms c_0 and m_0. The effective damping and mass coefficients are then written as:

$$m(x) = m_0(x) + 0.6\rho_{liq}L_i^{0.5}w^{1.5} \tag{22}$$

$$c = c_0 + 3\pi\eta + \frac{3}{4}\pi w^2\sqrt{2\eta\rho_{liq}\Omega} \tag{23}$$

To examine the resonant behavior and mass-sensing performance of the proposed MC, a modal analysis is carried out on the basis of the governing equation of motion. Because the sensing mechanism depends on the shift in the resonance characteristics after nanoparticle adsorption, the natural frequencies and mode shapes of the MC are determined first. The displacement field is expanded in terms of the vibration modes and their generalized coordinates as:

$$v(x,t) = \sum_{n=1}^{\infty}\psi_n(x)q_n(t) \tag{24}$$

where $\psi_n(x)$ is the nth mode shape of the MC and $q_n(t)$ is the corresponding generalized modal coordinate.

The MC is non-uniform because of the piezoelectric layer and the narrowed tip region, so it is divided into three uniform beam segments. The variation of bending stiffness and mass distribution among these segments must therefore be included in the modal formulation. For this purpose, the mode shape is defined piecewise over the three regions as

$$\psi_n(x) = \begin{cases} A_{n1}\,Sin\,\beta_{n1}x + B_{n1}\,Cos\,\beta_{n1}x + C_{n1}\,Sinh\,\beta_{n1}x + D_{n1}\,Cosh\,\beta_{n1}x & 0 < x < L_1 \\ A_{n2}\,Sin\,\beta_{n2}x + B_{n2}\,Cos\,\beta_{n2}x + C_{n2}\,Sinh\,\beta_{n2}x + D_{n2}\,Cosh\,\beta_{n2}x & L_1 < x < L_2 \\ A_{n3}\,Sin\,\beta_{n3}x + B_{n3}\,Cos\,\beta_{n3}x + C_{n3}\,Sinh\,\beta_{n3}x + D_{n3}\,Cosh\,\beta_{n3}x & L_2 < x < L \end{cases} \tag{25}$$

where A_{ni}, B_{ni}, C_{ni}, and D_{ni} are the unknown coefficients associated with the ith beam segment, and the corresponding wavenumber parameter is defined as $\beta_{ni} = \sqrt[4]{\rho A\omega_n^2/K}$.

The unknown coefficients in Eq. (25) are found by enforcing the clamped condition at the fixed end, the boundary conditions at the free end, and the continuity conditions at the junctions between adjacent segments. The mode shapes are then normalized using the adopted mass-normalization condition.

By inserting the modal expansion of Eq. (24) into the governing equation of motion and exploiting the orthogonality of the mode shapes, the spatial dependence is removed. The resulting equation is multiplied by the corresponding mode shape and integrated over the length of the MC, which gives the following ordinary differential equation for the *n*th modal coordinate:

$$\frac{d^2 q_n}{dt^2} + \omega_n^2 q_n + \mu_n \frac{dq_n}{dt} = \Gamma_n P(t) \tag{26}$$

where μ_n is the modal damping ratio, and

$$\omega_n^2 = \int_0^L \psi_n(x) \frac{d^2}{dx^2}\left[K(x)\frac{d^2\psi_n(x)}{dx^2}\right] dx \tag{27}$$

$$\Gamma_n = -\int_0^L \psi_n(x) \frac{d^2 C_P(x)}{dx^2} dx \tag{28}$$

The modal formulation accounts for the non-uniform bending stiffness, the distributed mass, the piezoelectric electromechanical coupling, and the concentrated mass of the adsorbed nanoparticle. The resulting modal equation therefore describes the dynamic response of the proposed resonant mass sensor directly in terms of its individual vibration modes.

The piezoelectric layer is driven by a harmonic voltage applied across the electrodes, so the electrical excitation is taken as $P(t) = P_0 \cos(\omega t)$, where P_0 is the excitation amplitude and ω is the excitation frequency. Under steady-state harmonic excitation, the generalized modal coordinate is assumed to be $q_n(t) = a_n \cos(\omega t)$, where a_n is the steady-state amplitude of the *n*th modal response.

Substituting the harmonic excitation and response into Eq. (26) and separating the harmonic terms gives the steady-state modal amplitude:

$$a_n = \frac{\Gamma_n P_0}{\sqrt{[(\omega_n^2 - \omega^2)^2 + (\mu_n \omega_n \omega)^2]}} \tag{29}$$

The resulting expression relates the excitation frequency, natural frequency, modal damping, and electromechanical coupling of the piezoelectric MC. In particular, the modal amplitude grows large as the excitation frequency approaches the corresponding natural frequency.

Because the proposed device works as a resonant mass sensor, the excitation frequency is chosen close to the natural frequency of the mode of interest, i.e., $\omega \approx \omega_n$. Under this resonant condition, the adsorption of a nanoparticle at the free end adds inertial loading and thereby shifts the natural frequency and modal response of the MC. The resulting resonance-frequency shift is the primary mass-sensing mechanism, while the associated changes in vibration amplitude and piezoelectric output can serve as complementary sensing signals.

4. Output Current of the Self-Sensing Piezoelectric Layer

Because the piezoelectric layer is used both as the actuator and as the sensor, the MC acts as a self-sensing, self-actuating mass sensor. The vibration of the MC strains the piezoelectric layer, which in turn generates an electrical current. Since this layer extends over the entire length of the MC, charge is produced continuously along the beam, and the output current is obtained by integrating the piezoelectrically induced response over the whole sensing region:

$$I(t) = -d_{31} E_p \, w_p \, z_p \, h_p \int_a^{L_1} \frac{\partial^3 v(x,t)}{\partial x^2 \, \partial t} \, dx \tag{30}$$

where d_{31} is the piezoelectric strain coefficient, and z_p is the distance between the mid-plane of the piezoelectric layer and the neutral axis. Applying the fundamental theorem of calculus reduces the spatial integral to the difference between the slope rates at the two ends of the sensing layer:

$$I(t) = d_{31} E_p \, w_p \, z_p \, h_p \frac{\partial^2 v}{\partial t \, \partial x}(L_1, t) \tag{31}$$

This result shows that the current is governed by the global deformation of the beam, namely the rate of change of the end slope, rather than by the local strain distribution within the piezoelectric layer. The formulation is thus considerably simplified while the electromechanical coupling mechanism is preserved.

Substituting the modal expansion into Eq. (24) gives

$$I(t) = d_{31} E_p \, w_p \, z_p \, h_p \frac{d\psi}{dx}(L) \frac{dq}{dt}(t) \tag{32}$$

The output current therefore consists of two factors: a structural factor, determined by the geometry, the electromechanical properties of the piezoelectric layer, and the modal slope at the free end, and a dynamic factor, the modal velocity. Both the structural design and the dynamic response thus influence the electrical performance of the sensor.

Under steady-state harmonic vibration, the modal coordinate varies harmonically, and the amplitude of the output current is

$$I_{\max} = d_{31} E_p \, w_p \, z_p \, h_p \, \frac{d\psi}{dx}(L) \, \omega_n a \tag{33}$$

where ω_n is the natural frequency of the considered mode and a is the modal vibration amplitude. According to Eq. (33), the current amplitude increases in proportion to the electromechanical coupling term, the frequency, the vibration amplitude, and the modal slope at the free end. Increasing any of these quantities therefore raises the electrical sensitivity of the sensor.

Eq. (33) links the mechanical vibration directly to the generated current. Since the adsorbed mass shifts ω_n and changes a, the current provides an electrical readout of the mass-sensing response, without any external displacement sensor. Because the model is simple and has a clear physical meaning, it is also well suited to comparing different substrate materials, piezoelectric materials, and structural configurations.

5. Numerical Simulation

The dynamic behavior and the self-sensing mass-detection performance of the proposed piezoelectric GPLRC MC are investigated with the theoretical model developed in the previous sections. The model is based on Hamilton's principle and Euler–Bernoulli beam theory, and it accounts for the multilayer structure, the piezoelectric actuation and sensing, and the adsorption of a nanoparticle at the free end.

The MC is a self-actuating, self-sensing device. An alternating voltage applied across the electrodes of the piezoelectric layer excites bending vibrations through electromechanical coupling, and the same layer converts the resulting vibration into an output current. The mass-sensing capability is evaluated by tracking how the resonant characteristics change when a nanoparticle adsorbs at the free end. The effects of the adsorbed mass on the resonance frequency, the frequency shift, and the output current are therefore examined systematically.

The geometric dimensions and material properties of the multilayer MC are listed in Tables 1 and 2, respectively. The electrodes are assumed to cover the piezoelectric layer completely, so their length and width equal those of the piezoelectric layer. The transverse piezoelectric coefficient is taken as d_{31} = 11 pC/N.

The functionally graded multilayer GPLRC layer is modeled as a nanocomposite of graphene platelets (GPLs) dispersed in an epoxy matrix. The GPLs have a length L_{GPL} = 2.5 μm, a width b_{GPL} = 1.5 μm, and a thickness t_{GPL} = 1.5 nm. Several GPL distribution patterns are considered in order to assess how the GPL arrangement affects the mechanical behavior, the dynamic response, and the mass-sensing performance of the MC. Unless stated otherwise, the polymer matrix is epoxy, and the GPL weight fraction is given as a percentage of the composite weight.

Table 1 Geometrical properties of the MC

	h (μm)	W (μm)	L (μm)
Tip	5.0	55	137
Base Layer	5.0	250	350
Piezoelectric Layer	5.0	130	330

Table 2 Material properties of the MC [32]

			E (Gpa)	ρ (Kg/m^3)
GPLRC	Matrix	Epoxy	3	1200
		Polypropylene	0.944	900
		Polyamide 6	2	1130
	GPL		1010	1062.5
Piezoelectric			180	2330

To accurately represent the functionally graded GPLRC layer as a multilayer structure, the number of layers must be large enough to capture the through-thickness variation of composition and effective properties. A natural-frequency convergence study was therefore carried out for different numbers of layers and GPL distribution patterns. The results show that 12 layers are sufficient to approximate the functionally graded GPLRC MC, since adding more layers changes the predicted natural frequencies only negligibly. Twelve layers are therefore used in all subsequent simulations, which balances computational cost and accuracy for all the GPLRC configurations considered.

To validate the analytical model, a dynamic micro-actuated silicon probe (DMASP) microcantilever manufactured by Veeco Instruments was used as the reference structure. Its experimental first-mode frequencies, measured before and after nanoparticle adsorption, are reported in [32].

The predictions are compared with the measurements in Table 3. Before mass deposition, the model gives 53.094 kHz against a measured 54.257 kHz (a difference of 2.189%). After adsorption, the corresponding values are 53.044 and 54.218 kHz (2.212%). The nearly identical deviations suggest a small systematic offset, plausibly caused by uncertainties in the reported dimensions and material properties and by the idealized clamped boundary, rather than by an error in the treatment of the adsorbed mass. The model also reproduces the adsorption-induced frequency decrease, which is 0.050 kHz in the prediction and 0.039 kHz in the experiment, an absolute difference of about 11 Hz. This agreement is important for a mass sensor, because the frequency shift, not the absolute frequency, is the quantity used to determine the adsorbed mass.

Table 3. Predicted and measured natural frequency (kHz) of the DMASP microcantilever before and after nanoparticle adsorption.

Condition	Measured [32]	Present model	Deviation (%)
Before mass deposition	54.257	53.094	2.189
After mass deposition	54.218	53.044	2.212

To verify the model for vibration in liquids with geometric discontinuity, the experimental results of Vázquez et al. [33] for the same DMASP microcantilever in water and in water–glycerol mixtures (10–40%) were also used. Table 4 compares the first-mode resonance frequency and amplitude. The deviations range from 0.3% to 2.3% in frequency and from 2.0% to 5.1% in amplitude, with the largest values in the 40% mixture. The model also follows the experimental trends. From water to the 40% mixture, the measured frequency drops from 16.00 to 14.88 kHz and the predicted one from 16.18 to 15.23 kHz, while the measured amplitude falls from 0.84 to 0.59 nm and the predicted one from 0.87 to 0.56 nm. These trends reflect the growing added fluid mass and viscous dissipation.

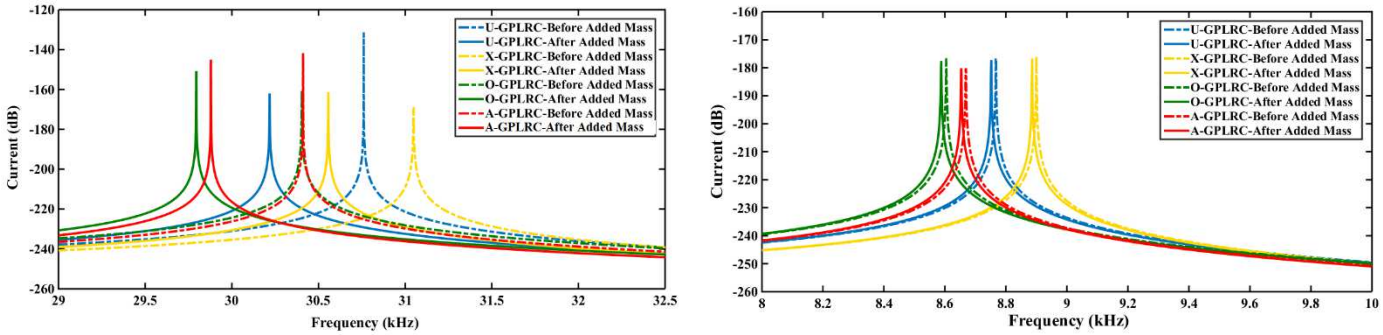
Overall, the agreement in air, before and after nanoparticle adsorption, and in liquids of different densities and viscosities shows that the proposed model predicts the dynamic behavior of the microcantilever reliably. It is therefore suitable for the analyses of the self-sensing mass sensor presented in the following sections.

Table 4. Comparison of the measured and predicted resonance frequency and amplitude of the DMASP microcantilever in water and water-glycerol mixtures.

Liquid medium	Frequency, measured [33] (kHz)	Frequency, present model (kHz)	Deviation (%)	Amplitude, measured [33] (nm)	Amplitude, present model (nm)	Deviation (%)
Water	16.00	16.18	1.1	0.84	0.87	3.5
Water-glycerol 10%	15.89	15.94	0.3	0.76	0.78	2.0
Water-glycerol 20%	15.64	15.75	0.7	0.72	0.70	2.8
Water-glycerol 30%	15.31	15.56	1.6	0.66	0.63	4.5
Water-glycerol 40%	14.88	15.23	2.3	0.59	0.56	5.1

With the model validated, this section examines how the self-sensing response of the MC depends on its design parameters, moving from the sensing mechanism to the design variables.

Figure 2 shows the frequency response of the output current before and after nanoparticle adsorption. In both media, adsorption shifts the resonance peak to a lower frequency and changes its height, which confirms that the output current of the piezoelectric layer can serve as the sensing signal without an external displacement sensor. The peak positions also depend on the GPL pattern. In air (Fig. 2a), the resonance occurs at about 29.8-31.1 kHz, with the X-GPLRC MC highest (about 31.1 kHz before adsorption) and the O-GPLRC MC lowest. This ordering is expected, because placing the GPLs in the outer layers (X) gives the stiffest laminate, whereas concentrating them near the mid-plane (O) gives the most flexible one. These shifts in resonance frequency and peak height are the origin of the change in output current. To compare configurations quantitatively, this change is expressed as the relative sensitivity $\Delta I/I$.



(a) (b)

Figure 2. Frequency response of the output current (dB) of the GPLRC MC before and after adsorption of a 20ng nanoparticle for different GPL patterns: (a) air and (b) water.

Since the peak positions and heights in Fig. 2 depend on the GPL pattern, the next step is to quantify how the polymer matrix and the pattern together control *ΔI/I*. Figure 3 compares the output-current change *ΔI/I* for three polymer matrices, epoxy, polyamide 6 (PA6), and polypropylene (PP), for all GPL patterns in air and water, at a GPL weight fraction of about 0.09%. In air, *ΔI/I* is only weakly dependent on the matrix, increasing slightly from epoxy to PA6 and PP for every pattern. For example, for O-GPLRC the values are about 20.5% for epoxy, 20.8% for PA6, and 22% for PP, whereas for X-GPLRC they are almost identical (about 11.8%) for all three matrices. The PP-based O-GPLRC MC reaches the highest sensitivity, about 22%. Among the patterns, O-GPLRC is the most sensitive (about 20.5-22%), followed by U-GPLRC and A-GPLRC (about 14-14.7%), and X-GPLRC is the least sensitive (about 11.8%) in air, which agrees with the stiffness ranking discussed above.

In water, *ΔI/I* is about one order of magnitude smaller (about 1.1-2.4%) than in air. The matrix effect remains weak and follows the same direction as in air, with ΔI/I increasing slightly from epoxy to PA6 and PP. The PP-based O-GPLRC MC is the most sensitive (about 2.4%), whereas the epoxy-based X-GPLRC MC is the least (about 1.15%). The strong reduction relative to air is attributed to the added fluid mass and viscous damping, which are dominant in water, so the particle mass is small relative to the total effective mass and the current change is reduced. In contrast to the matrix, the pattern has a clear effect, and the pattern ranking in water is the same as in air: O-GPLRC is the most sensitive and X-GPLRC the least for each matrix, with U-GPLRC and A-GPLRC in between (about 1.4-1.6%).

Hence, the GPL pattern is a more important design parameter than the matrix material, and the highest sensitivity in both media is obtained with the O-GPLRC pattern, with the softer PP matrix giving a small additional improvement. The much lower sensitivity in water is governed mainly by the fluid loading rather than by the choice of matrix.

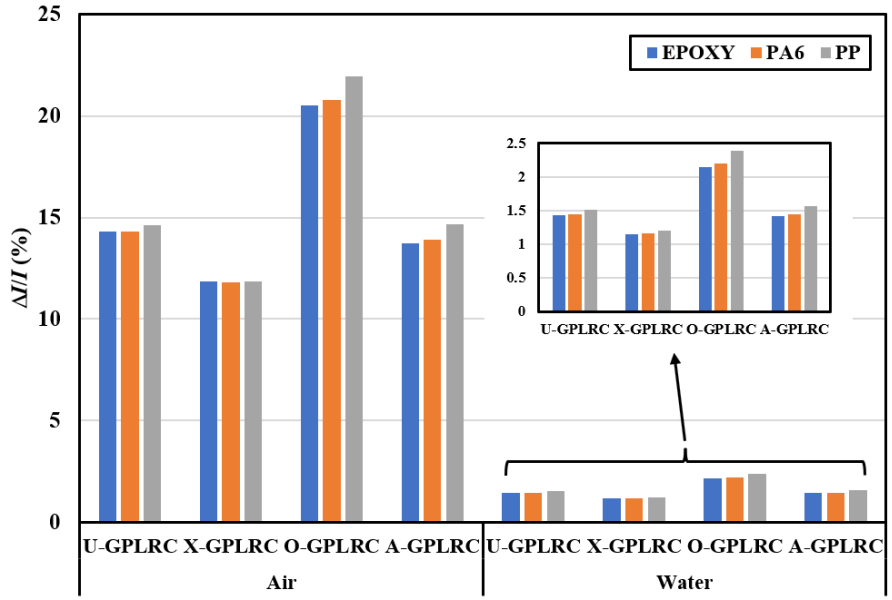


Figure 3. Effect of the polymer matrix (epoxy, PA6, PP) on the output-current change (*ΔI/I*) of the GPLRC MC for different GPL patterns after adsorption of a 20ng nanoparticle in air and water.

Since *ΔI/I* is already small in water, it is important to know how the sensitivity evolves as the liquid becomes denser and more viscous. Figure 4 shows the combined effect of the liquid (water and water–glycerol mixtures with 10–40% glycerol, at the same GPL weight fraction as in Fig. 3), the polymer matrix, and the GPL pattern on *ΔI/I*. Across all media, *ΔI/I* decreases steadily as the glycerol content increases. For example, for the PP-based O-GPLRC MC it falls from about 2.4% in water to about 2.1% in the 40% mixture, and for the epoxy-based X-GPLRC MC from about 1.15% to about 1.0%. This is a reduction of about 11% in both cases, which means that the liquid affects all configurations in nearly the same proportion. The reason is that the higher density and viscosity of the mixtures increase the added fluid mass and the viscous damping, so the same 20 ng particle produces a smaller relative change in the output current.

The ranking of the patterns and matrices does not depend on the liquid. In every medium, O-GPLRC is the most sensitive pattern and X-GPLRC the least, with U-GPLRC and A-GPLRC in between and close to each other, which agrees with Fig. 3. The matrix has only a small effect: the values for epoxy and PA6 are almost the same, and PP gives slightly higher values for all patterns (for O-GPLRC in water, about 2.15%, 2.2%, and 2.4% for epoxy, PA6, and PP, respectively). The highest sensitivity, about 2.4%, occurs for the PP-based O-GPLRC MC in water, whereas the lowest, about 1.0%, occurs for the epoxy-based X-GPLRC MC in the 40% mixture.

Therefore, the best liquid-phase performance is obtained with the O-GPLRC pattern, with PP giving a small additional improvement, and the sensitivity of all configurations is best preserved in low-viscosity media.

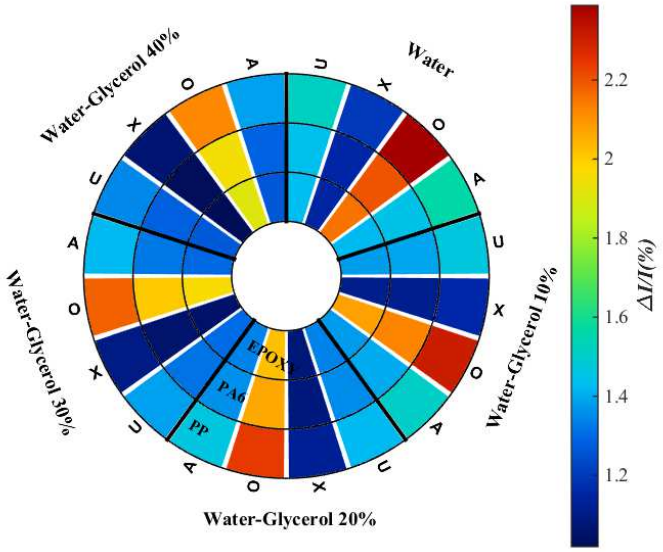
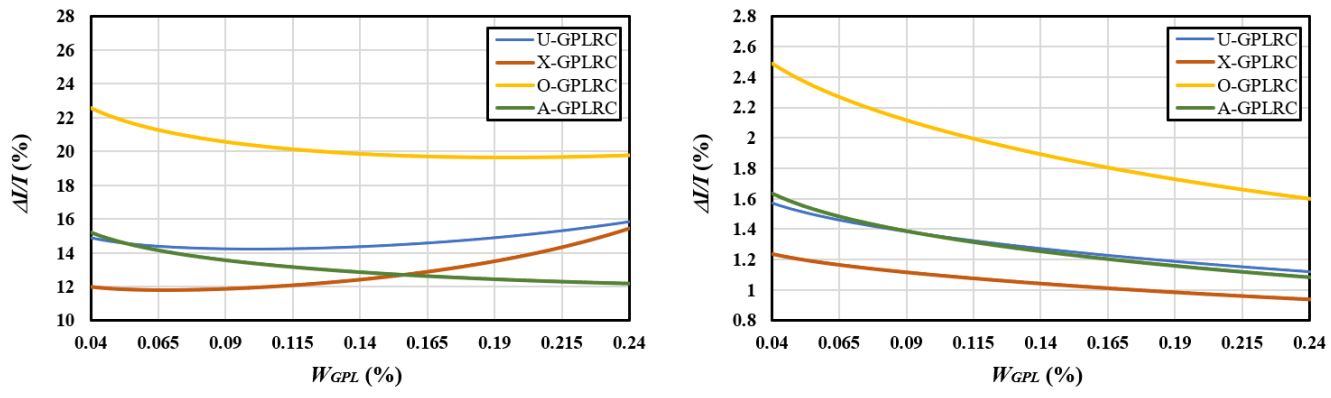


Figure 4. Effect of liquid medium, polymer matrix (epoxy, PA6, PP; inner to outer rings), and GPL pattern (U, X, O, A) on *ΔI/I* after adsorption of a 20ng nanoparticle.

Figure 5 shows the effect of the GPL weight fraction W_{GPL} (0.04–0.24%) and the GPL pattern on *ΔI/I* for the epoxy-based MC after a 20ng nanoparticle adsorbs at the free end. In air (Fig. 5a), *ΔI/I* lies between about 11.8% and 22.5% and depends strongly on the pattern. The O-GPLRC MC is the most sensitive over the whole range. Its ΔI/I decreases from about 22.5% at W_{GPL} = 0.04% to about 19.7% near 0.2% and then stays almost constant. The U-GPLRC MC passes through a shallow minimum of about 14.2% near 0.1% and then rises slightly to about 15.8%. The A-GPLRC MC decreases monotonically from about 15.2% to 12.2%. The X-GPLRC MC stays near 12% up to $W_{GPL} \approx 0.09\%$ and then increases to about 15.4%, overtaking the A-GPLRC MC at about 0.15% and approaching the U-GPLRC MC at the highest content. The ranking of the patterns other than O-GPLRC therefore depends on the GPL content: at low content it is O > A ≈ U > X, and at high content it is O > U ≈ X > A.

In water (Fig. 5b), *ΔI/I* is about an order of magnitude smaller (about 0.9–2.5%) and decreases monotonically with W_{GPL} for all patterns. The O-GPLRC MC decreases from about 2.5% to 1.6%, the U- and A-GPLRC MCs are almost identical and decrease from about 1.6% to 1.1%, and the X-GPLRC MC decreases from about 1.24% to 0.94%. The ranking O-GPLRC > U-GPLRC ≈ A-GPLRC > X-GPLRC is the same at all contents. This ranking follows the laminate bending stiffness: placing the GPLs in the outer layers (X-GPLRC) gives the stiffest MC and the lowest sensitivity, whereas concentrating them near the mid-plane (O-GPLRC) gives the most flexible MC and the highest sensitivity. The lower sensitivity compared with air is attributed to the added fluid mass and viscous damping. Hence, the O-GPLRC pattern gives the highest *ΔI/I* in both media, and a low GPL content is the most favorable in water.



(a) (b)

Figure 5. Effect of GPL weight fraction on the output-current change ($\Delta I/I$) after adsorption of a 20ng nanoparticle for different GPL patterns: (a) air and (b) water.

6. Sensitivity Analysis

The Sobol method is a global sensitivity analysis technique that quantifies the influence of input parameters on a model response over their entire prescribed ranges. It is particularly suitable for complex nonlinear problems in which the response depends simultaneously on several parameters and their interactions. The method provides quantitative measures of both the individual contributions of the input parameters and their interaction effects on the output variance.

In this study, the Sobol method is employed to investigate the sensitivity of the output current of the GPLRC mass microsensor to its geometrical parameters. The output current is selected as the response variable because the current change, ΔI/I, is the sensing indicator used to evaluate the performance of the microsensor in the preceding analyses. Based on the results presented earlier, the O-GPLRC pattern showed the highest sensitivity in both air and water and is therefore selected for the sensitivity analysis. The matrix material is polypropylene (PP), and the GPL weight fraction is fixed at $W_{GPL} = 0.065\%$.

The Saltelli sampling scheme with normally distributed input variables is employed [30] to calculate the total-order Sobol sensitivity indices. A sample size of N = 62000 is adopted to ensure statistically reliable estimates. To assess convergence, the sample size is progressively increased, and the computed indices are monitored until they stabilize, with negligible changes as N grows. Based on this assessment, N = 62000 is used for the final analysis. The total-order Sobol indices quantify the overall contribution of each input parameter to the variance of the output current, including both its direct effect and its interactions with the other parameters. A higher index indicates a stronger influence on the variability of the output current. In this section, the GPL length, width, and thickness are denoted by aGPL, bGPL, and tGPL, respectively (LGPL, bGPL, and hGPL in Section 2).

Figure 6 shows the variation of the output-current change $\Delta I/I$ in air with the GPL geometrical parameters for the four GPL patterns: the length a_{GPL} (Fig. 6a), the width b_{GPL} (Fig. 6b), and the thickness t_{GPL} (Fig. 6c). The scattered points are the sampled responses generated by the Saltelli scheme, and the solid curves show the corresponding mean trends. In all cases, the O-GPLRC pattern gives the highest $\Delta I/I$ and X-GPLRC the lowest, while U-GPLRC and A-GPLRC lie in between and are close to each other. This ranking is consistent with Fig. 3 and does not change over the investigated ranges of the parameters.

As shown in Fig. 6a, increasing a_{GPL} from 1 to 25 μm reduces $\Delta I/I$. The decrease is sharper at small lengths and gradually levels off beyond about $a_{GPL} \approx 15$ μm. For O-GPLRC, $\Delta I/I$ decreases from about 25% to about 22.5%, whereas for U-GPLRC and A-GPLRC it decreases from about 16-17% to about 15%. For X-GPLRC the change is very small, from about 12.6% to 11.8%. A similar behavior is seen in Fig. 6b for b_{GPL}, but the effect is stronger: for O-GPLRC, ΔI/I drops from about 26.5% to a minimum of about 22% near $b_{GPL} \approx 19$ μm and then rises slightly, while U-GPLRC and A-GPLRC decrease from about 17-18% to about 14.5-15%, and X-GPLRC from about 13% to 11.7%. The scatter of the data is also much larger at small a_{GPL} and b_{GPL}, which indicates that the response is more variable and more sensitive to these parameters when the GPLs are small.

In contrast, Fig. 6c shows that $\Delta I/I$ increases with the GPL thickness t_{GPL}, almost monotonically over the range of 1-57 nm. For O-GPLRC, $\Delta I/I$ rises from about 20.3% to about 25.5%, and for U-GPLRC and A-GPLRC from about 13.7% to 16-17%, with A-GPLRC slightly above U-GPLRC at large thicknesses. X-GPLRC shows the weakest dependence, increasing from about 11.3% to 12.7%. The scatter also grows with t_{GPL}, especially for U-GPLRC and A-GPLRC, which reflects stronger interaction with the other input parameters at larger thicknesses.

Overall, *ΔI/I* in air is reduced by larger GPL length and width and increased by larger GPL thickness. The O-GPLRC pattern, which concentrates the GPLs near the mid-plane, is the most sensitive to these parameters, whereas X-GPLRC, with the GPLs in the outer layers, is the least.

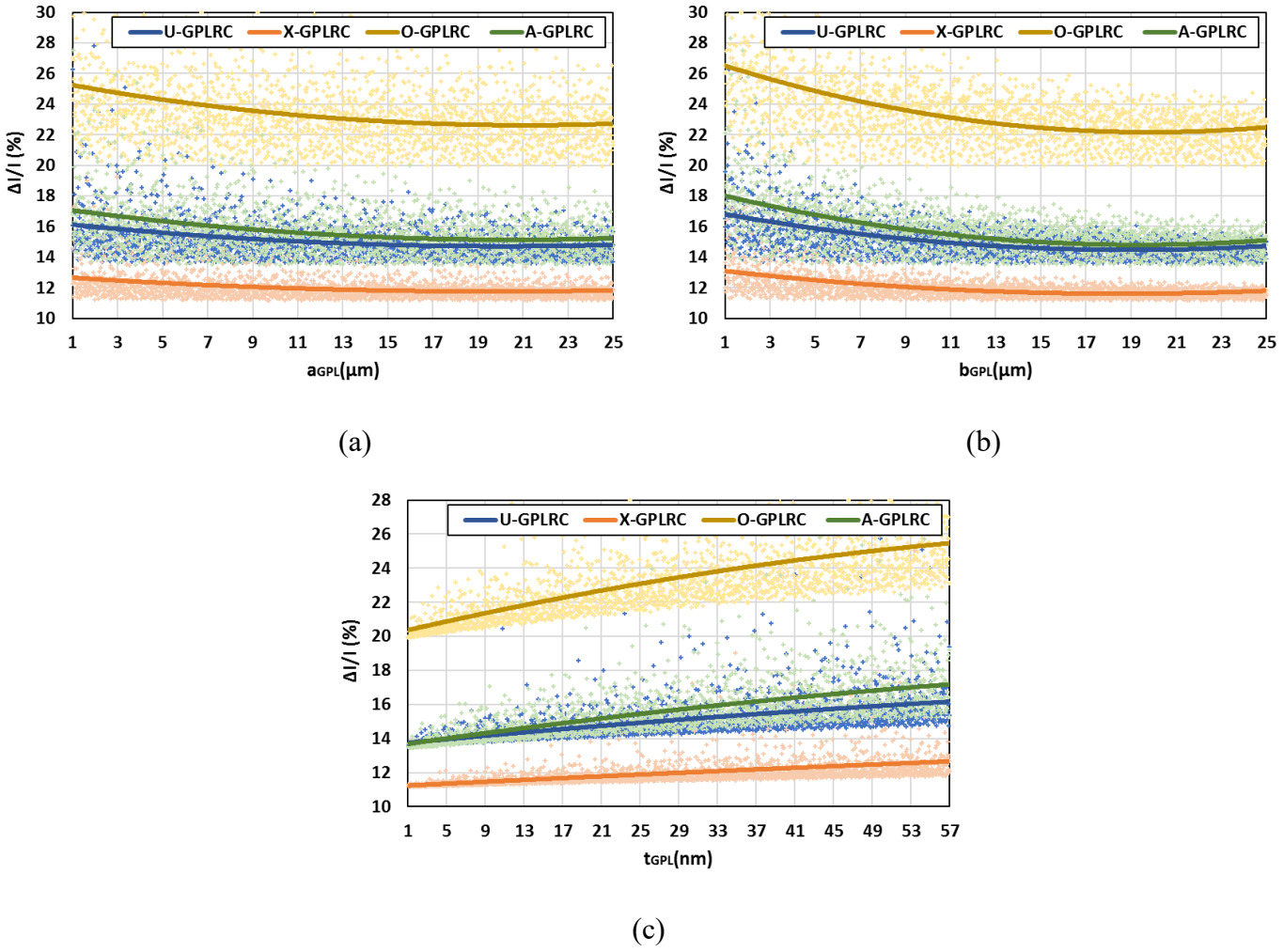


Figure 6. Effect of the GPL (a) length, (b) width, and (c) thickness on ΔI/I of the GPLRC microsensors in air.

Figure 7 shows the variation of *ΔI/I* in water with the GPL length a_{GPL} (Fig. 7a), width b_{GPL} (Fig. 7b), and thickness t_{GPL} (Fig. 7c) for the four GPL patterns. The pattern ranking is the same as in air: O-GPLRC is the most sensitive, X-GPLRC the least, and U-GPLRC and A-GPLRC lie in between. However, ΔI/I is about one order of magnitude smaller than in air (about 1-2.7% compared with 12-26%) because of the added fluid mass and viscous damping.

The trends with the GPL dimensions are also the same as in air. Increasing a_{GPL} and b_{GPL} reduces *ΔI/I*, with a sharper decrease at small values and a plateau at larger values. For O-GPLRC, *ΔI/I* decreases from about 2.55% to 2.25% with a_{GPL} and from about 2.7% to 2.2% with b_{GPL}, while the effect on X-GPLRC is much smaller (about 1.2% to 1.1%). The scatter is largest at small a_{GPL} and b_{GPL}, indicating a more variable response for small GPLs. In contrast, *ΔI/I* increases almost monotonically with t_{GPL} (Fig. 7c); for O-GPLRC it rises from about 2.0% to 2.6%, and for X-GPLRC from about 1.05% to 1.2%.

Overall, larger GPL length and width reduce the sensitivity in water, whereas larger thickness increases it, but the absolute variations are small because of the fluid loading.

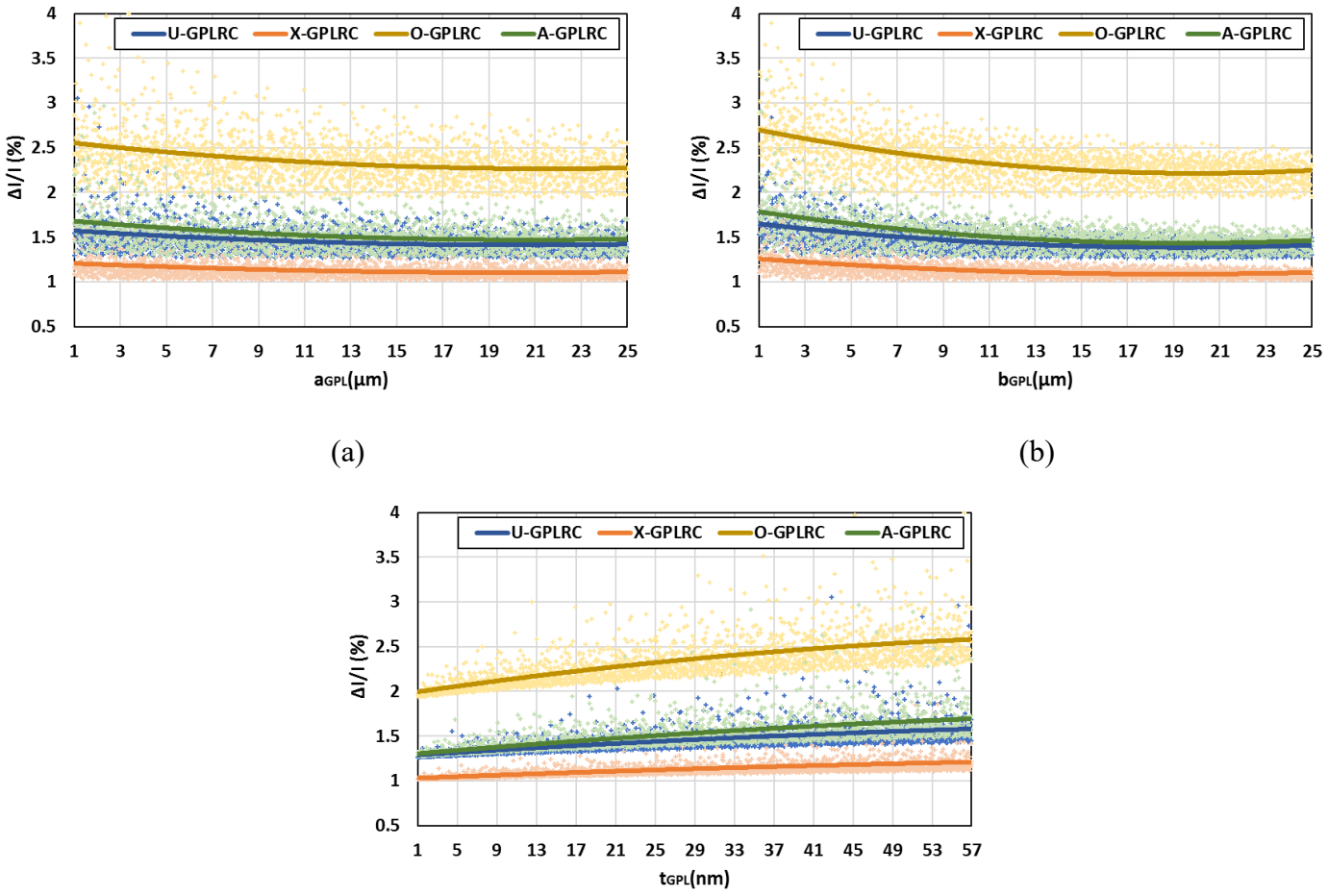


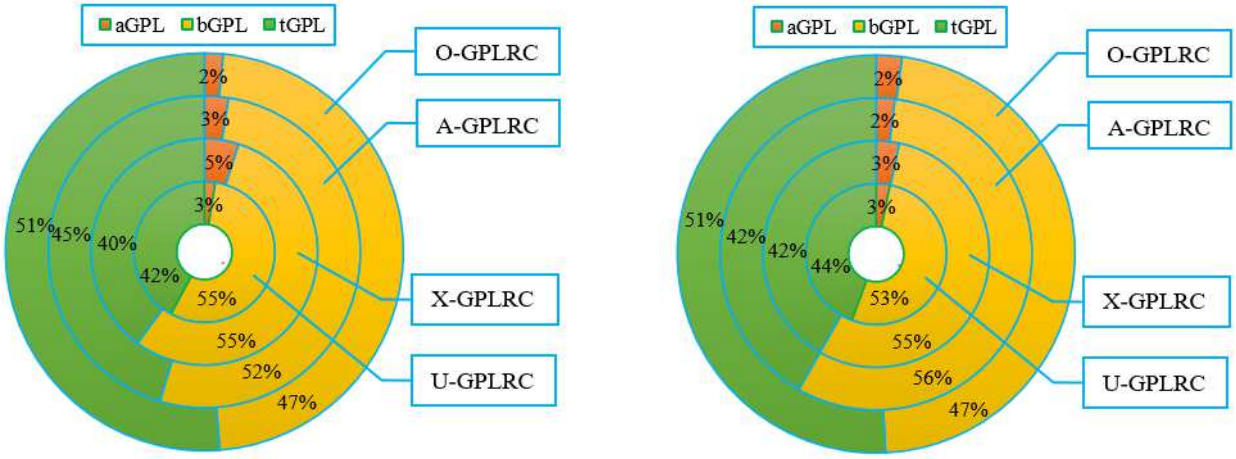
Figure 7. Variation of $\Delta I/I$ in water with the GPL (a) length, (b) width, and (c) thickness for the U-, X-, O-, and A-GPLRC patterns

Figure 8 shows the total-order Sobol indices of the GPL length a_{GPL}, width b_{GPL}, and thickness t_{GPL} for the output-current change $\Delta I/I$ of the four GPL patterns, in air (Fig. 8a) and in water (Fig. 8b). The indices are normalized so that they sum to 100% for each pattern. In both media, the length a_{GPL} has a negligible influence, with a contribution of only 2-5% for all patterns. The variance of $\Delta I/I$ is governed almost entirely by the width b_{GPL} and the thickness t_{GPL}.

In air (Fig. 8a), b_{GPL} is the dominant parameter for U-GPLRC (55%), X-GPLRC (55%), and A-GPLRC (52%), with t_{GPL} contributing 42%, 40%, and 45%, respectively. For O-GPLRC the two parameters are nearly balanced, with t_{GPL} slightly more influential (51%) than b_{GPL} (47%). The a_{GPL} index is highest for X-GPLRC (5%) and lowest for O-GPLRC (2%).

The results in water (Fig. 8b) are very similar to those in air. For O-GPLRC, t_{GPL} (51%) again slightly exceeds b_{GPL} (47%), whereas for the other patterns b_{GPL} remains dominant: U-GPLRC (53%), X-GPLRC (55%), and A-GPLRC (56%). The contribution of t_{GPL} is 44%, 42%, and 42%, respectively, and that of a_{GPL} is 2-3%. The medium therefore changes the indices by only a few percent and does not alter the ranking of the parameters.

These results agree with Figs. 6 and 7, where ΔI/I changed most strongly with b_{GPL} and t_{GPL} and only weakly with a_{GPL}. They indicate that, for the PP-based O-GPLRC microsensor, the GPL thickness and width should be the primary design parameters for tuning the sensitivity, whereas the GPL length can be fixed without significant loss of accuracy.



(a) (b)

Fig. 8. Total-order Sobol indices of a_{GPL}, b_{GPL}, and t_{GPL} for $\Delta I/I$ of the GPLRC microsensors in (a) air and (b) water. From the center outward, the rings correspond to U-, X-, A-, and O-GPLRC.

7. Conclusions

In this study, a self-actuating, self-sensing piezoelectric microcantilever with a multilayer GPLRC host structure was modeled for mass sensing in air and in liquid, and the relative change of the output current, $\Delta I/I$, was used as the sensing indicator. The main conclusions are as follows.

1. The proposed model, which includes the geometric discontinuities, the piezoelectric coupling, and the hydrodynamic loading, agrees well with experiments. The deviation in the first-mode frequency in air is about 2.2%, and in water and water–glycerol mixtures the deviations are 0.3–2.3% in frequency and 2.0–5.1% in amplitude. The model also reproduces the small frequency decrease caused by the adsorbed mass.

2. The output current of the piezoelectric layer can serve as the sensing signal without any external displacement sensor. Adsorption of a nanoparticle shifts the current resonance peak to a lower frequency and changes its height. In air, the resonance occurs at about 29.8–31.1 kHz, with the X-GPLRC MC the highest and the O-GPLRC MC the lowest, in agreement with the stiffness of the laminates.

3. Sensitivity is much lower in liquid than in air. For a 20ng particle, $\Delta I/I$ reaches about 22% in air but only 1.1–2.4% in water at a GPL weight fraction of about 0.09%, because the added fluid mass and viscous damping reduce the relative effect of the particle. It decreases further as the glycerol content, and hence the density and viscosity of the liquid, increases.

4. The GPL pattern is a more important design parameter than the polymer matrix. The O-GPLRC pattern gives the highest $\Delta I/I$ in both air and water, followed by U- and A-GPLRC, and X-GPLRC is the least sensitive. The matrix has only a small effect, and the softer polypropylene gives a slight improvement over epoxy and PA6.

5. The GPL weight fraction affects $\Delta I/I$ but does not change the best pattern. In air, $\Delta I/I$ of the O-GPLRC MC decreases from about 22.5% to 19.7% as W_{GPL} increases from 0.04% to 0.24%, whereas that of the X-GPLRC MC increases from about 12% to 15.4%. In water, $\Delta I/I$ decreases monotonically with W_{GPL} for all patterns. The O-GPLRC pattern is the most sensitive at all contents in both media, and a low GPL content is favorable in water.

6. The GPL dimensions have a clear influence on the response. Larger GPL length and width reduce $\Delta I/I$, with the sharpest change at small sizes, whereas larger GPL thickness increases it. The trends are the same in air and in water, although the absolute changes are much smaller in water.

7. The Sobol analysis for the PP-based O-GPLRC microsensor shows that the variance of $\Delta I/I$ is governed almost entirely by the GPL width and thickness. For the O-GPLRC pattern, the thickness contributes about 51% and the width 47%, and for the other patterns the width is slightly dominant. The GPL length contributes only 2–5%, and the medium changes the indices by only a few percent. The GPL width and thickness should therefore be the primary design parameters, while the length can be fixed.

These findings can guide the selection of the GPL pattern and geometry for resonant mass sensors in air and in liquid. Future work should include experimental validation of the GPLRC microcantilever itself, the effect of the position of the adsorbed mass, and the use of higher vibration modes.

Funding Declaration

The authors received no financial support for the research, authorship, and/or publication of this article.

References

[1] Johnson, B.N. and R. Mutharasan, Biosensing using dynamic-mode cantilever sensors: A review. Biosensors and bioelectronics, 2012. **32**(1): p. 1–18.
[2] Ghaemi, N., A. Nikoobin, and M.R. Ashory, A comprehensive categorization of micro/nanomechanical resonators and their practical applications from an engineering perspective: a review. Advanced Electronic Materials, 2022. **8**(11): p. 2200229.
[3] Darban, H., Size effect in ultrasensitive micro-and nanomechanical mass sensors. Mechanical Systems and Signal Processing, 2023. **200**: p. 110576.
[4] Rahmani, A., A. Babaei, and S. Faroughi, Vibration characteristics of functionally graded micro-beam carrying an attached mass. Mechanics of Advanced Composite Structures, 2020. **7**(1): p. 49–58.
[5] Formica, G., W. Lacarbonara, and H. Yabuno, Nonlinear dynamic response of nanocomposite microbeams array for multiple mass sensing. Nanomaterials, 2023. **13**(11): p. 1808.
[6] Shahraki, Z.N. and R. Ghaderi, Vibration and sensitivity analysis of piezoelectric microcantilever as a self-sensing sensor. The European Physical Journal Applied Physics, 2019. **87**(2): p. 20401.
[7] Ghaderi, R. and H. Safari, Dynamic and sensitivity analysis of V-shaped cross section piezoelectric beam as mass sensor for high-order vibration modes. Journal of Mechanical Engineering and Sciences, 2025: p. 10770–10781.
[8] Ghaderi, R. and M.S. Tehrani, Torsional vibration and sensitivity analysis of microcantilever in liquid. Latin American Applied Research-An international journal, 2024. **54**(1): p. 127–132.
[9] Lee, C., et al., Measurement of the elastic properties and intrinsic strength of monolayer graphene. science, 2008. **321**(5887): p. 385–388.
[10] Reif, J., et al., Enhanced mechanical properties of nanocomposites at low graphene content. ACS nano, 2009. **3**(12): p. 3884–3890.
[11] Islam, M.H., et al., Graphene and CNT-based smart fiber-reinforced composites: a review. Advanced Functional Materials, 2022. **32**(40): p. 2205723.
[12] Kumar, A., K. Sharma, and A.R. Dixit, A review on the mechanical properties of polymer composites reinforced by carbon nanotubes and graphene. Carbon letters, 2021. **31**(2): p. 149–165.
[13] Choudhary, M., et al., Contemporary review on carbon nanotube (CNT) composites and their impact on multifarious applications. Nanotechnology Reviews, 2022. **11**(1): p. 2632–2660.
[14] Bilisik, K. and M. Akter, Graphene nanoplatelets/epoxy nanocomposites: a review on functionalization, characterization techniques, properties, and applications. Journal of Reinforced Plastics and Composites, 2022. **41**(3-4): p. 99–129.
[15] Lapčík, L., et al., Study of mechanical properties of epoxy/graphene and epoxy/halloysite nanocomposites. Nanotechnology Reviews, 2023. **12**(1): p. 20220520.

[16] Madhad, H.V., et al., Graphene/graphene nanoplatelets reinforced polyamide nanocomposites: A review. High performance polymers, 2021. **33**(9): p. 981–997.
[17] Zhao, S., et al., Functionally graded graphene reinforced composite structures: A review. Engineering Structures, 2020. **210**: p. 110339.
[18] Wu, H., J. Yang, and S. Kitipornchai, Mechanical analysis of functionally graded porous structures: A review. International Journal of Structural Stability and Dynamics, 2020. **20**(13): p. 2041015.
[19] Feng, C., S. Kitipornchai, and J. Yang, Nonlinear free vibration of functionally graded polymer composite beams reinforced with graphene nanoplatelets (GPLs). Engineering Structures, 2017. **140**: p. 110–119.
[20] Song, M., S. Kitipornchai, and J. Yang, Free and forced vibrations of functionally graded polymer composite plates reinforced with graphene nanoplatelets. Composite Structures, 2017. **159**: p. 579–588.
[21] Wang, Y., et al., Nonlinear static and dynamic responses of graphene platelets reinforced composite beam with dielectric permittivity. Applied Mathematical Modelling, 2019. **71**: p. 298–315.
[22] Allahkarami, F. and H. Tohidi, Size-dependent nonlinear free vibration of multilayer functionally graded graphene nanocomposite Timoshenko microbeam under different boundary conditions. The European Physical Journal Plus, 2021. **137**(1): p. 5.
[23] Liu, D., et al., State-space formulation for buckling and free vibration of axially functionally graded graphene reinforced nanocomposite microbeam under axially varying loads. Materials, 2024. **17**(6): p. 1296.
[24] Koppanati, M.S., M. Naga Rani, and K. Krishna Bhaskar, Free vibration analysis of graphene reinforced laminated composite plates using experimental modal testing. Mechanics of Advanced Composite Structures, 2023. **10**(2): p. 363–374.
[25] Mao, J., et al., Vibrations of graphene nanoplatelet reinforced functionally gradient piezoelectric composite microplate based on nonlocal theory. Composite Structures, 2020. **236**: p. 111813.
[26] Abbaspour, F. and H. Arvin, A free vibration analysis of laminated microplates reinforced by graphene platelets integrated with piezoelectric facesheets, resting on an elastic foundation, and subjected to thermoelectrical loads. Mechanics of Composite Materials, 2022. **58**(3): p. 435–450.
[27] Chen, J., X. Zhang, and M. Fan, Dynamic behaviors of graphene platelets-reinforced metal foam piezoelectric beams with velocity feedback control. Applied Mathematics and Mechanics, 2025. **46**(1): p. 63–80.
[28] Nguyen, V.-L., et al., Electro-thermal vibration of graphene platelets reinforced functionally graded piezoelectric microplates under different boundary conditions. International Journal of Solids and Structures, 2025. **314**: p. 113273.
[29] Mazari, M.Y., et al., Integrating machine learning with vibration analysis for graphene platelet nanocomposite beams subjected to magnetic loading. Mechanics of Advanced Materials and Structures, 2026. **33**(1): p. 2476785.
[30] Saltelli, A., et al., Variance based sensitivity analysis of model output. Design and estimator for the total sensitivity index. Computer physics communications, 2010. **181**(2): p. 259–270.
[31] Rankl, C., et al., Hydrodynamic damping of a magnetically oscillated cantilever close to a surface. Ultramicroscopy, 2004. **100**(3-4): p. 301–308.
[32] Salehi-Khojin, A., et al., Nanomechanical cantilever active probes for ultrasmall mass detection. Journal of Applied Physics, 2009. **105**(1).
[33] Vazquez, J., et al., Dynamic response of low aspect ratio piezoelectric microcantilevers actuated in different liquid environments. Journal of Micromechanics and Microengineering, 2009. **19**(1): p. 015020.